Modern Physics Letters B
(2023) 2350216 (22 pages)

DOI: 10.1142/S0217984923502160

World Scientific
www.worldscientific.com

High-sensitivity ring-core photonic crystal fiber sensor based on surface plasmon resonance for ultra-low refractive index detection

Luhui Xu*, Chao Peng*, Tongyu Meng†, Ying Shi‡, Qiang Liu*, Jingwei Lv*, Wei Liu*, Paul K Chu§ and Chao Liu*,¶

*School of Physics and Electronic Engineering,
Northeast Petroleum University,
Daqing 163318, China

†Leicester International Institute,
Dalian University of Technology,
Dalian 124221, China

‡Institute of Unconventional Oil and Gas,
Northeast Petroleum University,
Daqing 163318, China

§Department of Physics,
Department of Materials Science and Engineering,
and Department of Biomedical Engineering,
City University of Hong Kong,
Tat Chee Avenue, Kowloon, Hong Kong, China
¶msm-liu@126.com

Received 10 April 2023
Revised 22 May 2023
Accepted 18 June 2023
Published 18 August 2023

A novel ring-core photonic crystal fiber (PCF) sensor based on surface plasmon resonance (SPR) is designed for ultra-low refractive index detection. A gold nanowire is coated on the outer surface of the PCF as a plasma material, greatly facilitating the manufacturing of the sensor. To achieve real-time detection, the analyte is located on the outside of the sensor. The mode coupling effect and main performance parameters are analyzed through finite element method. In addition, by optimizing several important structural parameters, the overall performance of the sensor has been greatly improved. The optimized sensor shows a maximum wavelength sensitivity of 26,000 nm/RIU in the refractive index range of 1.14–1.26, maximum amplitude sensitivity of 300 RIU^{-1}, as well as minimum resolution of 3.85×10^{-6} RIU. The PCF-SPR sensor with outstanding properties has great potential in applications such as oil logging, biosensing, and chemical monitoring.

Keywords: Optical fiber sensing; surface plasmon resonance; photonic crystal fiber; low refractive index sensing.

¶Corresponding author.

1. Introduction

Optical fiber sensing has experienced tremendous progress in recent years, especially in communication and sensing. The former requires a high capacity and quality, while the latter needs a high detection sensitivity and wide detection range.[1–3] Compared to communication, optical fiber sensing is more diverse, and many types of optical fiber devices have been developed based on different optical theories. The basic principle is to establish the correlation between the spectra and certain characteristics of the external medium by detecting the spectral changes in the transmitted light beams in the optical fiber.

Surface plasmon resonance (SPR) has received much attention recently. When a light beam impinges onto a metal surface, a surface plasma polariton (SPP) is excited and coupled with an evanescent wave generated by total internal reflection under certain conditions. The coupling parameters change with the refractive index of the surrounding medium and hence, SPR has been used for sensing.[4,5] Conventional SPR sensors are mostly of the prismatic type and typical configurations are the Otto and Kretschmann types.[6,7] However, this type of SPR sensor has a large volume and low sensitivity and is not suitable for most applications. By coating or filling the plasmonic materials in the optical fiber, the SPP mode can be excited under certain conditions to produce SPR and a sharp loss curve in the spectrum. Since changes of the characteristics of external media change the loss curve, the characteristics can be assessed spectroscopically.[8,9]

Different types of fibers can be used in SPR sensing. However, the single-mode fiber has limited transmission modes and design freedom. The photonic crystal fiber (PCF) is a micro-structured optical fiber showing the refractive index difference between the core and cladding layer by putting periodic pores in the bulk materials.[10–13] In this way, the light beam is constrained in the PCF fiber core and traverses in a stable manner. Although the PCF structure is more complex than that of traditional optical fibers, it creates more freedom for the design and application leading to better characteristics and structural diversity.[14–17]

According to the placement of the analyte, PCF-SPR sensors are generally divided into two types,[18] internal and external. In the internal sensor, analytes fill the air holes in the PCF and the detection sensitivity is higher. However, filling or coating analytes and plasmonic materials inside the microstructures is difficult in practice and real-time monitoring cannot be easily achieved thus hampering commercial application. On the other hand, an external sensor is easier to produce by coating the plasmonic medium on the surface of the PCF and surrounding the analyte around the optical fiber. Hence, the external sensor is more suitable for real-time monitoring and has more practical significance.

Currently, many external optical fiber SPR sensors incorporate the use of gold nanowires. Yan *et al.*[19] proposed a PCF-SPR liquid sensor in which two gold coatings with nanowires are deposited symmetrically on the PCF to achieve a wavelength sensitivity of 9200 nm/RIU in the refractive index range of 1.33–1.36. Zhan *et al.*[20]

designed a micro-structured optical fiber SPR sensor wrapped with gold nanowires and in the refractive index range of 1.33–1.40, the maximum wavelength sensitivity reaches 12,314 nm/RIU. Tong *et al.*[21] proposed a D-type dual-core PCF-SPR sensor based on metal nanowires. The sensor consists of a polished D-type dual-core photonic crystal fiber and a metal nanowire array, and in the refractive index range of 1.32–1.38, a maximum wavelength sensitivity of 16,000 nm/RIU is observed. Pan *et al.*[22] designed a localized SPR refractive index sensor based on PCF on which 31 silver nanowires are placed on the D-shape PCF. The simulation results indicate that the maximum sensitivity is 16,400 nm/RIU in the refractive index range of 1.26–1.33. However, existing sensors of this type have low sensitivity or a small range of refractive indexes, resulting in poor overall performance. In addition, it is worth noting that there are few external high-performance PCF-SPR sensors available for low refractive index detection.

Herein, a ring-core PCF-SPR sensor designed for the detection of low refractive indexes is analyzed by the finite element method (FEM) implemented in COMSOL Multiphysics. The results show that the ring-core structure constrains the light field making it closer to the gold nanowires coated on the outer surface to enhance coupling between the fundamental mode and SPP mode. The sensor exhibits a maximum wavelength sensitivity of 26,000 nm/RIU and maximum amplitude sensitivity of 300 RIU^{-1} in the refractive index range of 1.14–1.26.

2. Basic Theory and Structure Optimization

The light beam traversing the PCF-SPR sensor excites SPPs in the vicinity of the metal coating and under certain conditions, the propagation constant of the core mode will be equal to that of the SPP mode on the metal surface resulting in SPR.[23,24] The beam maintains a specific field distribution as it propagates through the fiber and will not change with distance. Each field distribution is referred to as an eigenmode and is a solution of the wave equation. According to the component of the electromagnetic field in the propagation direction, the eigenmodes can be divided into the TE, TM, EH, and HE modes. The longitudinal electric field component of the TE mode is 0 and the longitudinal magnetic field component of the TM mode is 0. The EH and HE modes with both the longitudinal magnetic and electric fields are called hybrid vector modes. In weakly guiding optical fibers, the propagation constants of these eigenmodes are very close, resulting in degeneration and a mode with almost constant polarization direction called the linearly polarized LP mode. In non-weakly guiding fibers, the eigenmodes can be separated and the fiber can transmit the fundamental mode $HE_{1,1}$ mode as well as other high-order eigenmodes.[25,26] However, the PCF does not have regular boundary conditions and cannot be solved analytically by the Helmholtz equation and therefore, the finite element analysis is commonly used to derive the mode field distribution.

The properties of the materials should be considered when designing and numerically analyzing the sensor. Silica is often used as the bulk material for PCF due

to its low cost and simple manufacturing. However, when light travels in a medium, the medium has different refractive indexes at different wavelengths, which is known as material dispersion. The dispersion of silica can be derived by the Sellmeier equation[27]:

$$n^2 - 1 = \frac{0.6961663\lambda^2}{\lambda^2 - 0.0684043^2} + \frac{0.4079426\lambda^2}{\lambda^2 - 0.1162414^2} + \frac{0.897479\lambda^2}{\lambda^2 - 9.896161^2}, \tag{1}$$

where n is the refractive index of silica and λ is the incident wavelength. The selection of plasma materials is also a critical factor in the design of the sensor. Gold, silver, copper, and aluminum are commonly used plasma materials that can effectively generate the SPR effect. However, gold has more stable chemical properties compared to other metals, which can ensure the normal operation of the sensor for a long time. And the ductility of gold is better, making it easier to manufacture and practical applications. Thus it is selected as the plasmonic medium and coated onto the surface of the optical fibers in the form of gold nanowires. The dielectric constant of gold for different wavelengths can be derived by the Drude–Lorentz model as follows[28]:

$$\varepsilon(\omega) = \varepsilon_\infty - \frac{\omega_p^2}{\omega(\omega + i\omega_c)}, \tag{2}$$

where $\varepsilon(\omega)$ is the dielectric constant of the metal, ε_∞ is related to the high-frequency absorption peak, ω_c is the collision frequency, and ω_p is the plasma frequency. For gold, $\varepsilon_\infty = 9.75$, $\omega_c = 1.45 \times 10^{14}\,\text{rad/s}$, and $\omega_p = 1.3659 \times 10^{16}\,\text{rad/s}$. The beam propagating through the fiber core by total internal reflection will generate evanescent waves on the metal surface. In addition, the surface plasma wave (SPW) is a charge density oscillation in the cross section between the metal film and the dielectric substrate. Only when the phase matching condition is met, the SPW will be excited by the external beam. However, the momentum of light in free space is smaller than that of SPW, resulting in momentum mismatch. This means that light beams in free space cannot directly excite SPW, while evanescent waves have this ability and can effectively form SPR effects under certain conditions.[4] In optical fibers, phase matching manifests as the equality of mode propagation constants. With changing wavelength, the propagation constant of the core mode will be equal to that of the SPP mode in the gold nanowires at a certain point as expressed by Eq. (3).[29]

$$k_{\text{Core}} = \frac{\omega_0}{c}\sqrt{\varepsilon_d}\sin\theta_{\text{SP}} = k_{\text{SP}}, \tag{3}$$

where ω_0 is the plasma frequency, c represents the speed of light in vacuum, ε_0 is the dielectric constant of the target medium, and θ_{SP} is the resonance angle. This means that the two modes couple strongly, and the photon energy in the core mode is transferred to the vicinity of the gold nanowires. As the wavelength approaches the phase matching point, the charge density oscillation on the metal surface is excited,

so the area of positive charge surplus exists in it. Under the action of Coulomb force, electrons in the fiber core are attracted to the vicinity of the metal and neutralized with positive charges, resulting in increased losses. As the wavelength continues to increase, the charge density oscillation on the metal surface gradually weakens, thus reducing the attraction of positive charges. The repulsive force between electrons will cause them to return to the fiber core, reducing the loss in the fiber. A loss peak thus appears from the spectrum, and the corresponding wavelength of the loss peak is called the resonance wavelength. The loss can be obtained by the following equation[30,31]:

$$L = 8.686 \times \frac{2\pi}{\lambda} \mathrm{Im}(n_{\mathrm{eff}}), \tag{4}$$

where λ is the wavelength and n_{eff} is the effective refractive index of the mode. The amplitude of the resonance wavelength corresponding to the refractive index of the analyte is an important criterion to evaluate the performance of the sensor and is expressed in terms of the wavelength sensitivity[32]:

$$S(\lambda) = \frac{\Delta\lambda_{\mathrm{peak}}}{\Delta n_a}, \tag{5}$$

where $\Delta\lambda_{\mathrm{peak}}$ is the resonant wavelength shift and Δn_a is the change in the refractive index of the analyte.

In this work, a new type of PCF-SPR sensor is designed. By using two layers of cladding air holes and a larger central air hole, a ring core is created in the PCF, in which the fundamental mode is constrained. Compared to the solid PCF, the ring-core structure reduces the area of the mode field and makes the photon energy more concentrated. Moreover, this structure guides the light field to be closer to the gold nanowires on the outer surface, making it easier for the fundamental mode to leak into the SPP to increase mode coupling. The cross-section of the designed sensor is shown in Fig. 1 in which the blue area represents silicon dioxide, the white area

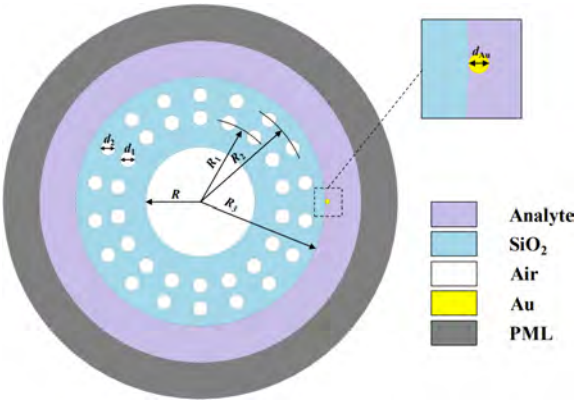

Fig. 1. (Color online) Cross-section of the circular PCF-SPR sensor.

represents the air hole, and the gold part is the gold nanowire coated onto the outer surface of the PCF. The analyte surrounds the external part of the sensor during operating as shown in the purple area in the figure. The radius of the central air hole is R. The first and second air holes are composed of 18 air holes with equal angular spacing and the center distances are R_1 and R_2, respectively. The diameters of the holes are d_1, d_2. The radius of the cladding is R_3, and a gold nanowire with a diameter of d_{Au} is coated on the outer surface of the cladding. The merit of this design is that the sensor has a simple structure and is easy to manufacture. In order to obtain the appropriate initial parameter values, a large number of rough simulation calculations are carried out, which ensures that the designed sensor can transmit mode stably and achieve the SPR effect. In addition, the extent to which each parameter affects the sensor performance is demonstrated in the process, and several important parameters will be further optimized for better performance.

In the preliminary study, the following parameters which enable the sensor to excite the SPR effectively are chosen: (1) center air hole radius $R = 7.4\,\mu$m, (2) center distance of the first layer air hole $R_1 = 13.8\,\mu$m, (3) center distance of the second layer air hole $R_2 = 17.6\,\mu$m, (4) cladding radius $R_3 = 20.6\,\mu$m, (5) diameter of the first air hole $d_1 = 2.6\,\mu$m, (6) diameter of the second air hole $d_2 = 3.2\,\mu$m, and (7) diameter of the gold line $d_{\mathrm{Au}} = 2\,\mu$m. By adopting these parameters, the fundamental mode $\mathrm{HE}_{1,1}$ is clustered in the ring core and propagates stably. However, the X polarization state and Y polarization state of the $\mathrm{HE}_{1,1}$ mode exhibit different effects when coupled to the SPP mode. As shown in Fig. 2, the electric field of $\mathrm{HE}_{1,1}$ mode is concentrated in the ring core and divided into two high electric field intensity regions with central symmetry. In addition, the transverse electric field component dominates in the mode field and has a unified direction. In the X polarization mode, the transverse electric field components all point towards the metal film, making it easier for the mode field in the ring core to transfer to the SPP mode. The X polarization of $\mathrm{HE}_{1,1}$ mode will have better SPR excitation effect in theory. In fact, the results in Fig. 2 indicate that X polarization shows an obvious mode field transfer process and strong coupling, whereas Y polarization hardly changes. Therefore, X polarization of the $\mathrm{HE}_{1,1}$ mode is used as the excitation mode. In addition, the refractive index range is 1.14–1.26 thus spanning the range of low refractive indexes.

At the initial structural parameters, the loss spectrum of the designed sensor within the entire refractive index detection range is shown in Fig. 2(c). The result reveals that the sensor with initial parameters has a good trend of loss peaks, but the overall wavelength sensitivity needs to be promoted. It achieves the highest wavelength sensitivity of 13,000 nm/RIU in the refractive index range of 1.25–1.26. In order to improve the properties, several important parameters are optimized in which process the wavelength sensitivity in the analyte refractive index range n_a of 1.25–1.26 is selected as the main optimization criterion, while also taking into the account other indicators such as the full-width at half-maximum (FWHM). Based on the degree of influence of parameters on sensor performance and structural characteristics, these important structural parameters are optimized in order from the

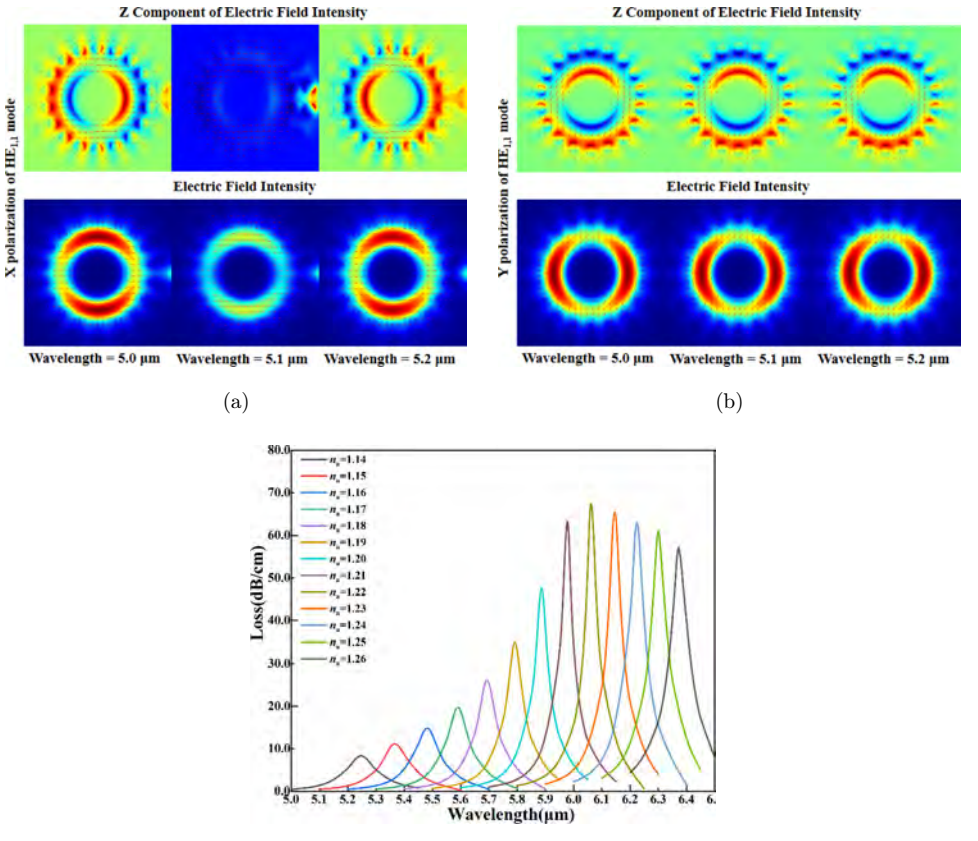

Fig. 2. (Color online) Mode field transfer processes: (a) X polarization and (b) Y polarization for the $HE_{1,1}$ mode; (c) Loss spectrum of the sensor at initial structural parameters.

inside out, which is the center air hole radius R, the first air hole diameter d_1, the second air hole diameter d_2, and the gold line diameter d_{Au}. In addition, when optimizing one parameter, keeping the other parameters unchanged not only ensures the optimization effect but also improves computational efficiency. Although this method omits some parameter combinations, it generally has little effect on the final optimization results.

The radius of the central air hole R is an important parameter that directly affects the mode field distribution. It not only determines the thickness of the ring core, but also changes the distance between the mode field and gold nanowire. Figure 3(a) depicts the changes in the loss spectrum as the central air hole radius R increases from 7.4 μm to 9 μm in steps of 0.4 μm. The resonance wavelength blue-shifts as R increases. The loss decreases and the resonance peak flattens gradually. Figure 3(b) shows the curve of the resonance wavelength and wavelength sensitivity in the refractive index range of 1.25–1.26. The larger the R, the greater the blueshift of the

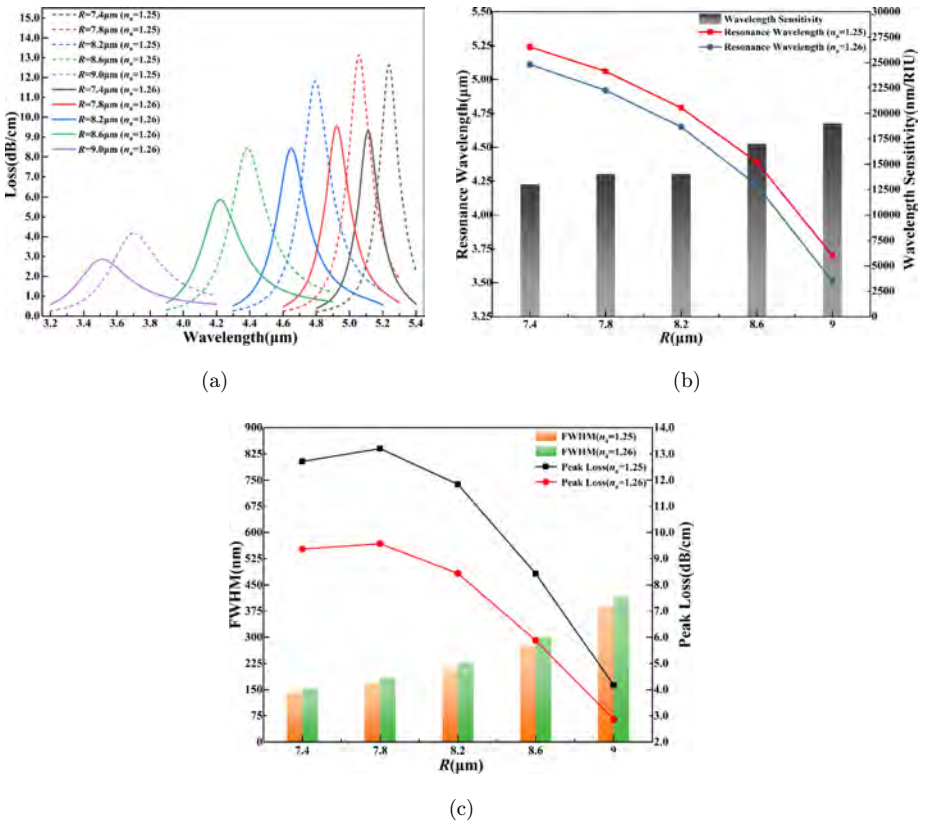

Fig. 3. (Color online) (a) Loss spectra, (b) wavelength sensitivity and resonance wavelength, and (c) FWHM and peak loss for different R and analyte refractive indexes of $n_a = 1.25$ and 1.26.

resonance wavelength and the higher the wavelength sensitivity. Accordingly, R should be as large as possible. However, it is necessary to ensure the quality of the loss curve while increasing the wavelength sensitivity. The FWHM and peak loss in Fig. 3(c) intuitively represent the sharpness of the loss curve. When R is 9 μm, the loss peak becomes relatively flat, and further increasing R leads to poor quality of the spectral curve during sensing consequently affecting the actual performance. In general, a larger radius of the central air hole decreases the thickness of the ring core and compresses the area of the mode field to produce less loss. However, it also brings the fundamental mode closer to the SPP mode and the external analyte to enhance mode coupling and improve the detection sensitivity. Therefore, the radius of the central air hole R is determined to be 9 μm and the wavelength sensitivity increases from 13,000 nm/RIU to 19,000 nm/RIU.

The first layer air hole diameter d_1 is the next parameter to be optimized. It determines the ability of the cladding to constrain the mode field. An excessively large d_1 decreases the gap between the first layer of the air holes and prevents the

mode field from leaking to the gold nanowires, thus limiting mode coupling. A small d_1 makes the mode field unrestricted resulting in unstable beam transmission. Based on the optimized center air hole radius R, the effects of the first layer air hole diameter d_1 are analyzed when it increases from 2.2 μm to 2.6 μm in 0.1 μm steps. Figure 4(a) shows the change of the loss curve, and a smaller d_1 gives rise to red-shifting of the resonance wavelength. Moreover, the loss increases due to more leakage of the mode field. Figure 4(b) presents the resonance wavelength and wavelength sensitivity for different d_1. It can be seen that the resonance wavelength bears an almost linear function relationship with d_1. When d1 is between 2.5 μm and 2.6 μm, the wavelength sensitivity remains at 19,000 nm/RIU but with decreasing d_1, the wavelength sensitivity drops slightly. On the other hand, according to the FWHM and peak loss in Fig. 4(c), the larger d_1, the sharper the loss curve. In order to achieve higher sensitivity while also taking into account the loss spectrum, $d_1 = 2.5\,\mu$m is chosen. In general, d_1 has little effect on the wavelength sensitivity, although it can alter the loss. The FWHM of the loss curve is improved by adjusting d_1, and the wavelength sensitivity remains at 19,000 nm/RIU.

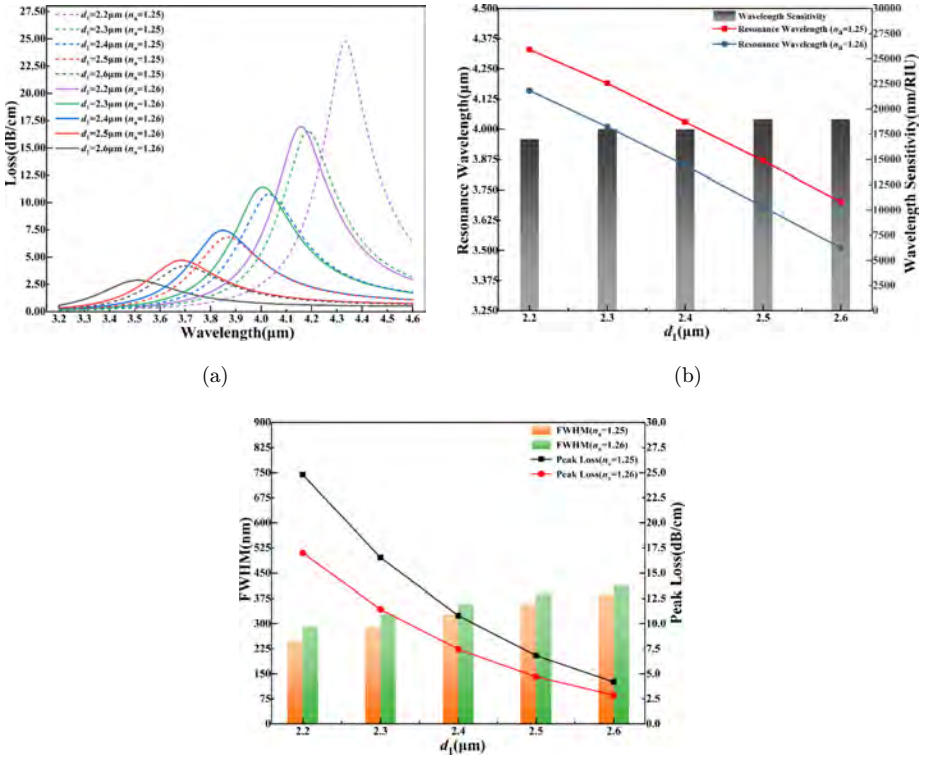

Fig. 4. (Color online) (a) Loss spectra, (b) wavelength sensitivity and resonance wavelength, and (c) FWHM and peak loss for different d_1 and analyte refractive index of $n_a = 1.25$ and 1.26.

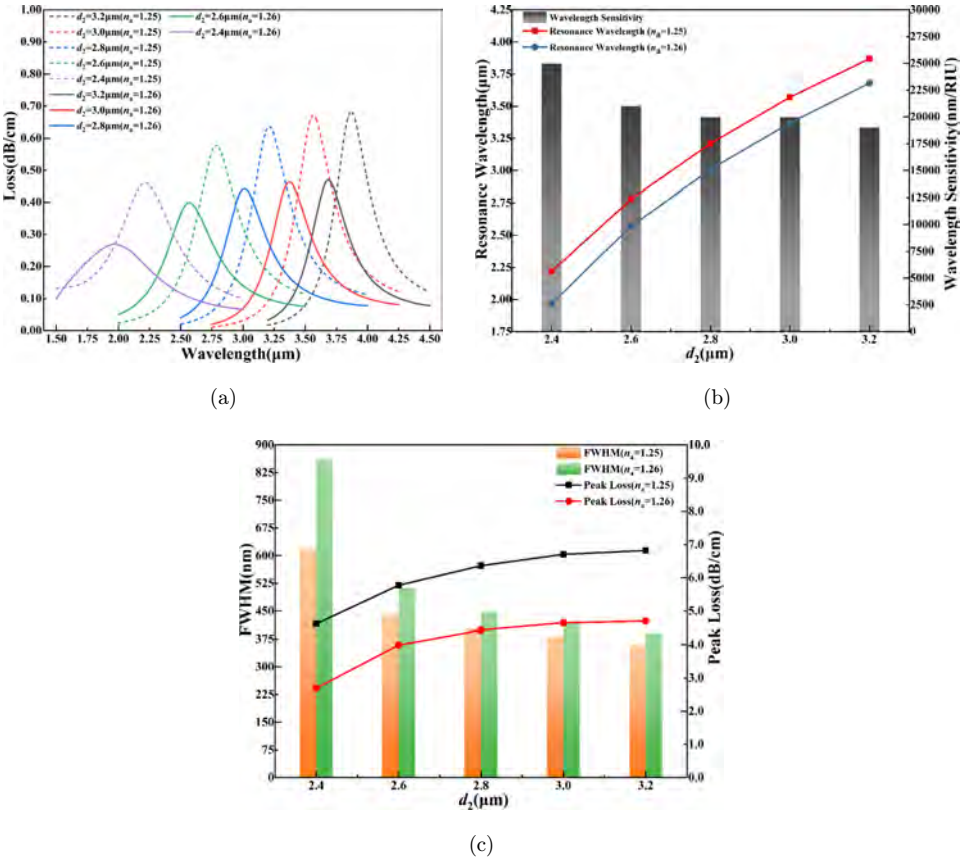

Fig. 5. (Color online) (a) Loss spectra, (b) wavelength sensitivity and resonance wavelength, and (c) FWHM and peak loss for different d_2 and analyte refractive indexes of $n_a = 1.25$ and 1.26.

Based on the optimized center air hole radius and first layer air hole diameter, the second layer air hole diameter d_2 is optimized. Figure 5(a) shows the change of the loss curve when d_2 decreases from 3.2 μm to 2.4 μm at steps of 0.2 μm. As d_2 decreases, the resonance wavelength changes. The loss also descends albeit insignificantly. Figure 5(b) describes the relationship between the second layer air hole radius d_2 and resonance wavelength and wavelength sensitivity. The curve of the resonance wavelength exhibits a large slope, implying that the second layer of air holes affects the refractive index difference between the PCF cladding and core, consequently changing the wave band of mode coupling. On the other hand, a smaller d_2 also increases the wavelength sensitivity. When d_2 decreases from 2.6 μm to 2.4 μm, the wavelength sensitivity increases dramatically to 25,000 nm/RIU. However, according to the rule described in Fig. 5(c), further reduction of d_2 leads to a large increase in the FWHM and a flat loss curve. Therefore, the diameter of the second layer air hole d_2 is adjusted to 2.4 μm. The wavelength sensitivity increases

from 19,000 nm/RIU to 25,000 nm/RIU and the resonance wavelength declines significantly from about 4 μm to 2 μm.

The diameter of the gold nanowires d_{Au} has a direct influence on SPP excitation and so their size is crucial. Here, several important changes are analyzed when the diameter of the gold nanowires d_{Au} decreases from 2 μm to 0.8 μm in steps of 0.4 μm. Figure 6(a) depicts the regularity of the loss peaks. Overall, the loss curve does not change significantly, although a smaller d_{Au} produces a small redshift of the resonance wavelength and increased loss. In addition, Fig. 6(b) shows that the wavelength sensitivity increases albeit in small increment, implying that smaller gold nanowire diameters result in greater sensitivity. However, when d_{Au} is less than 1.2 μm, the wavelength sensitivity remains at 26,000 nm/RIU. The relationship between d_{Au} and FWHM and peak loss in Fig. 6(c) shows that the FWHM tends to decrease with decreasing gold nanowire diameter d_{Au}, while the peak loss goes up. All in all, changing d_{Au} to 0.8 μm improves the wavelength sensitivity and increases the sharpness of the loss peaks. On the other hand, the size of gold nanowires has little

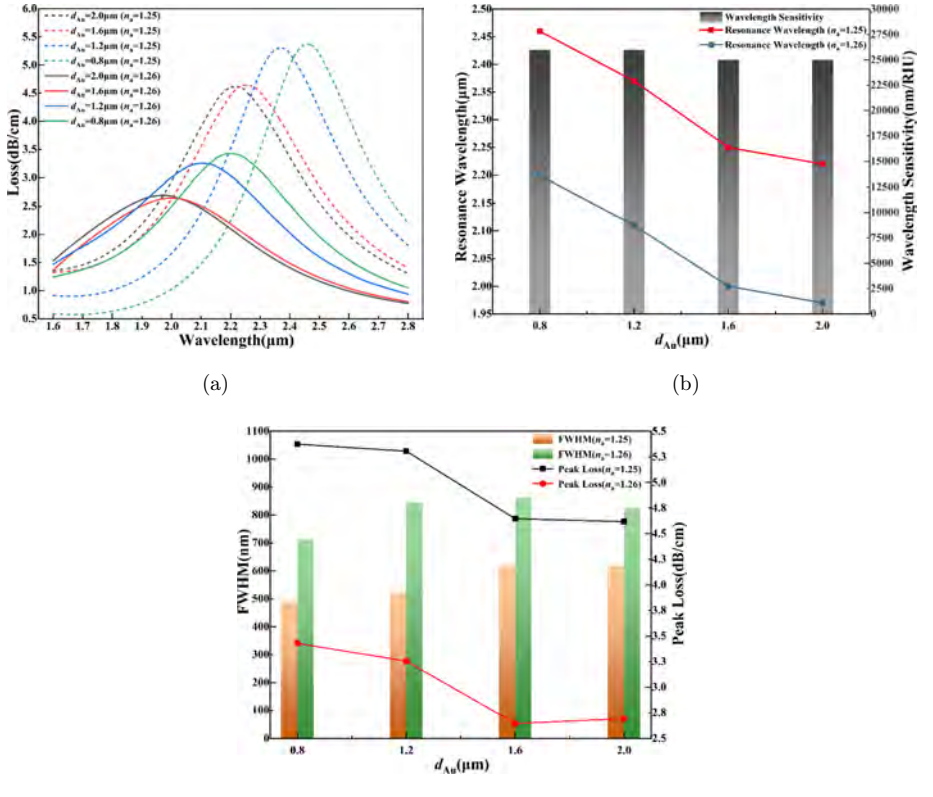

Fig. 6. (Color online) (a) Loss spectra, (b) wavelength sensitivity and resonance wavelength, and (c) FWHM and peak loss for different d_{Au} and analyte refractive indexes of $n_a = 1.25$ and 1.26.

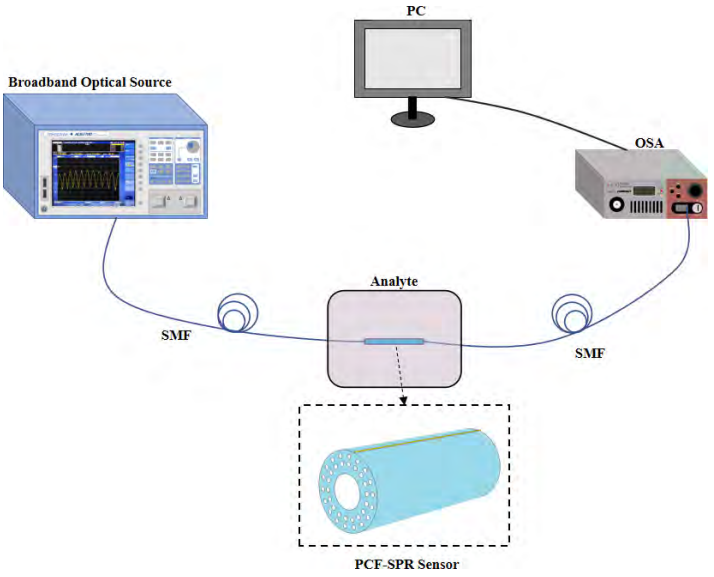

Fig. 7. (Color online) Schematic diagram showing the sensing process.

influence on the sensing properties, thus increasing the tolerance of manufacturing errors.

By optimizing the aforementioned parameters, that is, $R = 9\,\mu$m, $d_1 = 2.6\,\mu$m, $d_2 = 2.5\,\mu$m, and $d_{\mathrm{Au}} = 0.8\,\mu$m the maximum wavelength sensitivity goes up from 13,000 nm/RIU to 26,000 nm/RIU.

This PCF-SPR sensor has a simple structure and gold nanowires are deposited onto the outer surface of the PCF to minimize production complexity. In practice, PCFs are generally produced by the catalyzed sol-gel method in which silica is converted into a sol and a gel is formed. After the heat treatment, the gel is processed into the optical fiber preform, and introduced into the wire drawing tower to form the required optical fiber shape.[33,34] The finished PCF is coated with gold nanowires to form the PCF-SPR sensor. As shown in Fig. 7, in the actual test, the sensor terminals are connected to the light source and optical spectrum analyzer (OSA) via a single-mode fiber (SMF), and the sensor is immersed directly in the analyte.

3. Results and Discussion

3.1. *Coupling properties*

After optimization, the sensor delivers not only high detection sensitivity, but also excellent performance. Adequate mode coupling is a prerequisite to achieving detection, and the PCF-SPR sensor exhibits good mode coupling effects. Figure 8 shows the effective refractive index curves of the fundamental mode and SPP mode near the resonant wavelength as well as the loss curve of the fundamental mode,

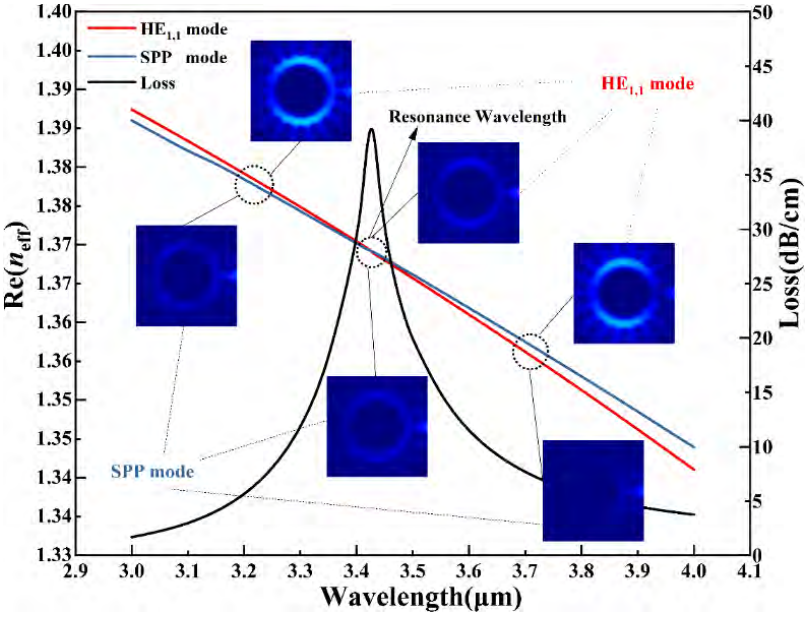

Fig. 8. (Color online) Dispersion curves and mode field distributions in phase matching.

when the refractive index of the analyte is 1.20. There is an intersection between the effective refractive index curve of the fundamental mode and the SPP mode, where the loss of the fundamental mode reaches a peak. This means that the fundamental mode and SPP mode couple well at this wavelength. Figure 8 describes the changes in the mode field during mode matching. Before the phase matching point, the base mode is bound in the ring core, and only a small portion of the light field leaks near the gold nanowires. At the resonance wavelength, a large portion of the light field in the fundamental mode is transferred to the vicinity of the gold nanowires, while the light field in the SPP mode concentrates at the ring core. Therefore, the mode field distribution of the fundamental mode is similar to that of the SPP mode at resonance. When the wavelength exceeds the resonant wavelength, the mode fields of the fundamental mode and SPP mode gradually revert to their original distributions. In fact, mode coupling is also a process of energy transfer. In order to quantify this process, we calculate the power fraction η of each region in the mode field at different wavelengths by Eq. (6)[35]:

$$\eta = \frac{\iint_X S_z dxdy}{\iint_{\mathrm{All}} S_z dxdy}, \tag{6}$$

where S_z represents the z component of the Poynting vector, the numerator is the optical power of each part, and the denominator is the total power of the fiber section. Figure 9 shows the power fraction curves of the core region and gold nanowire region of the fundamental mode during mode coupling. The power fraction

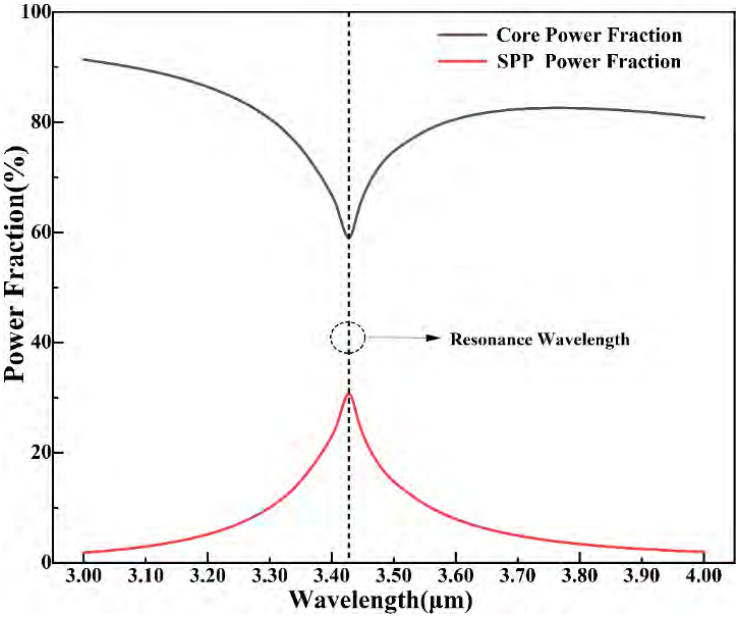

Fig. 9. (Color online) Mode power fractions in phase matching.

of the gold nanowire region in the fundamental mode is away from the resonance wavelength, indicating that the mode field is concentrated in the core with little transfer. As the wavelength approaches the resonant wavelength, the power fraction in the core region decreases gradually and reaches a trough at the resonant wavelength, while the power fraction in the gold nanowire region reaches a peak. This trend corresponds to the process shown in Fig. 8 and explains mode coupling in the sensor from another perspective.

3.2. *Loss spectrum and wavelength sensitivity*

It is important to establish the relationship between the refractive index of the analyte and loss spectrum. Figure 10 shows the loss spectrum in the refractive index range between 1.14 and 1.26 and it shows good regularity. As the refractive index of the analyte decreases, the resonance wavelength red-shifts. The loss increases sharply and then decreases slightly. The FWHM and peak loss are also shown in Fig. 10. FWHM decreases and then increases, reaching the smallest value of 136.8 nm at a refractive index of 1.20. This means that when the refractive index is around 1.20, the loss peak is the sharpest and the sensor delivers the best performance. Moreover, based on the loss spectrum, Fig. 11 calculates the resonance wavelength and wavelength sensitivity for different analyte refractive indexes. The detection sensitivity of the sensor changes for analytes with different refractive indices. Within the entire refractive index detection range, the higher the refractive index of the analyte, the higher the wavelength sensitivity of the sensor. The maximum wavelength

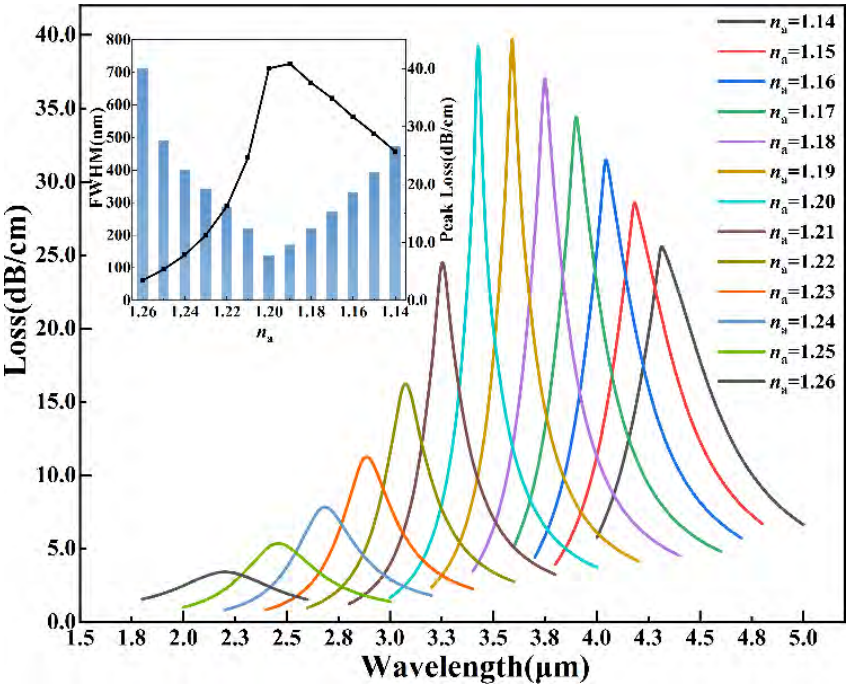

Fig. 10. (Color online) Loss curves for analyte refractive indexes between 1.14 and 1.26.

sensitivity of 26,000 nm/RIU is achieved within the refractive index detection range of 1.25 to 1.26. The average wavelength sensitivity within the entire detection range has also reached 17,583.3 nm/RIU. The wavelength sensitivity response represents the rate of change of the resonance wavelength with the refractive index of the analyte. This trend reveals that the change of the resonance wavelength is closer to a conical curve than a linear one. Therefore, the curve of the resonance wavelength with refractive index is fitted by a quadratic function as shown in Fig. 11. The curve agrees well with the actual data and reflects the effects of the resonance wavelength change, which can improve the accuracy in actual detection. The empirical fit is as follows:

$$\lambda_{\text{peak}} = -43386.3 + 95298.2n_a - 46903.1n_a^2. \tag{7}$$

3.3. *Amplitude sensitivity*

Amplitude detection at a specific wavelength is another method to measure the sensing sensitivity. In practice, owing to the wide refractive index detection range and large resonance wavelength range, it is difficult to determine the wavelength sensitivity. Therefore, monitoring the loss changes of different analytes at fixed wavelengths is a more effective method to evaluate the sensor sensitivity represented

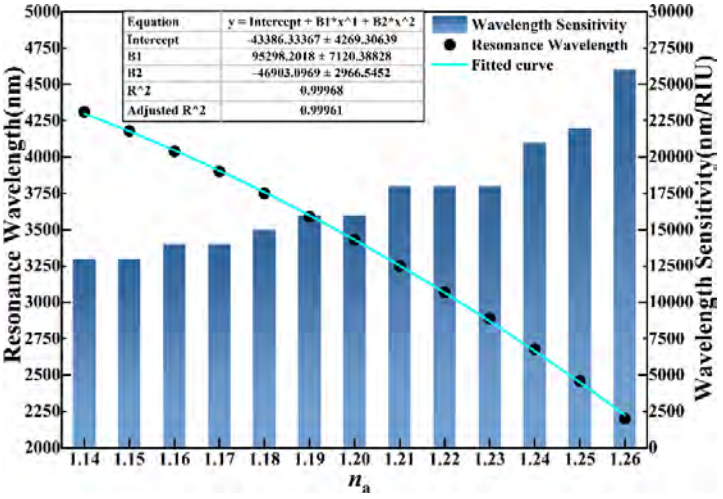

Fig. 11. (Color online) Linear fitting between the resonance wavelength and refractive index of the analyte for the PCF-SPR sensor.

by the amplitude sensitivity, as shown in Eq. (8)[36]:

$$S_A(\lambda) = -\frac{1}{\alpha(\lambda, n_a)} \frac{\partial \alpha(\lambda, n_a)}{\partial n_a}, \tag{8}$$

where $\alpha(\lambda, n_a)$ is the confinement loss when the refractive index of the analyte is n_a, $\partial\alpha(\lambda, n_a)$ is the difference between two adjacent loss spectra caused by the small change of the refractive index of the analyte, and ∂n_a is the change of the refractive index of the analyte.

Figure 12 shows the amplitude sensitivity of the sensor for different analyte refractive indexes. The amplitude sensitivity corresponding to the refractive index of each analyte increases initially and then decreases with red-shifting of the wavelength and there is a maximum. On the other hand, when the refractive index is between 1.25 and 1.19, the maximum amplitude sensitivity rises significantly with decreasing refractive indexes. When the refractive index of the analyte decreases from 1.19 to 1.14, the maximum amplitude sensitivity decreases significantly and throughout the entire refractive index detection range, the sensor shows a maximum amplitude sensitivity of 300 RIU^{-1} for $n_a = 1.19$.

3.4. *Resolution*

Resolution refers to the minimum change in the refractive index a sensor can detect and to a certain extent reflects the detection accuracy of the sensor. It can be calculated by Eq. (9)[37]:

$$R = \frac{\Delta\lambda_{\min}}{S(\lambda)}, \tag{9}$$

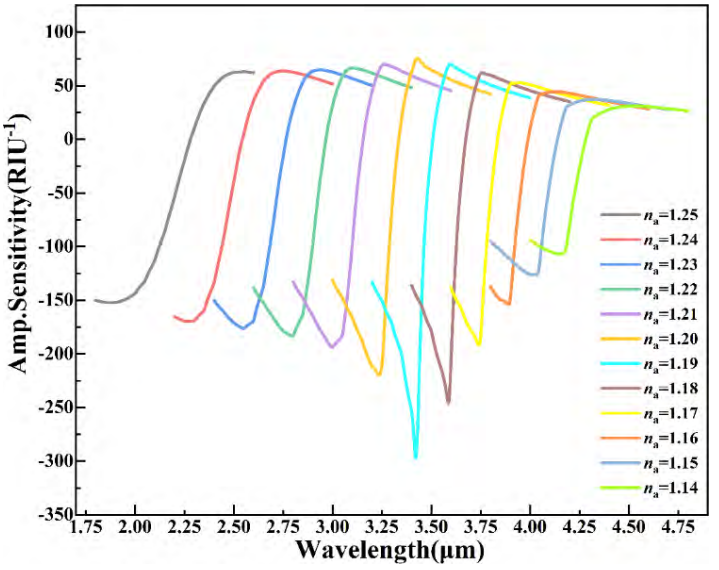

Fig. 12. (Color online) Variation of the amplitude sensitivity with wavelength.

where the minimum resolution of wavelength $\Delta\lambda_{\min} = 0.1\,\text{nm}$. The resolution may fluctuate for different refractive index ranges and Fig. 13 shows the resolution corresponding to the refractive indexes of different analytes. It can be seen that the resolution decreases with increasing analyte refractive indexes. This means that the higher the refractive index, the lower the detection limit of the sensor. When $n_a = 1.26$, the resolution of the sensor reaches a minimum of 3.85×10^{-6} RIU.

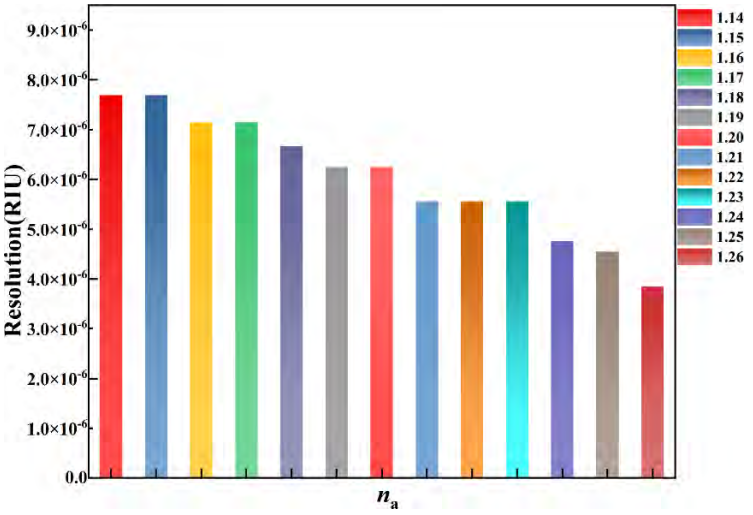

Fig. 13. (Color online) Resolution of the PCF-SPR sensor.

3.5. *Detection distance*

In practice, the stability of mode transmission is important. The walk-off length represents the maximum distance the mode can transmit stably and improving the detection distance is of great significance. The walking distance can be calculated by Eq. (10)[38]:

$$L_{10\,\mathrm{ps}} = \frac{c \times 10\,\mathrm{ps}}{n_{\mathrm{eff}}^{\mathrm{even}} - n_{\mathrm{eff}}^{\mathrm{odd}}} = \frac{3 \times 10^{-3}}{n_{\mathrm{eff}}^{\mathrm{even}} - n_{\mathrm{eff}}^{\mathrm{odd}}}, \tag{10}$$

where c is the speed of light, and $n_{\mathrm{eff}}^{\mathrm{even}}$ and $n_{\mathrm{eff}}^{\mathrm{odd}}$ are the effective refractive indexes of the even and odd modes, respectively. Here, we analyze the mode walk-off lengths of different analytes at the resonance wavelengths, as shown in Fig. 14. The detection distance of the sensor increases gradually with increasing analyte refractive indexes. When the refractive index of the analyte is less than 1.20, the walk-off length is less than 30 m. When the refractive index is higher than 1.20, the walk-off length increases dramatically to a maximum of 1187 m. This indicates that the higher the refractive index of the analyte, the longer the detection distance and the better the overall performance.

3.6. *FOM and SNR*

The PCF-SPR sensor detects the refractive index of the analyte by locating the loss peak and therefore, the quality of the loss spectrum is an important indicator of the

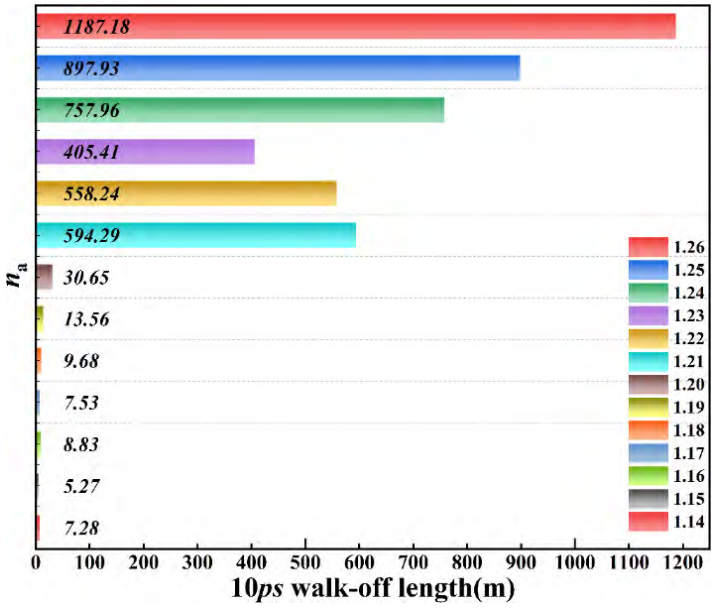

Fig. 14. (Color online) 10 ps walk-off length of the fundamental mode of the PCF-SPR sensor for different n_a.

sensor performance. A high-quality loss curve is beneficial to locating the resonance wavelengths and improving the detection accuracy. The figure of merit (FOM) is an evaluation index that measures the overall quality of the loss spectrum and it includes factors such as wavelength sensitivity and FWHM as follows[39]:

$$\mathrm{FOM} = \frac{S(\lambda)}{\mathrm{FWHM}}, \tag{11}$$

where S is the wavelength sensitivity of different analytes and FWHM is the full-width at half-maximum. The signal-to-noise ratio (SNR) is another indicator to evaluate the quality of the loss spectrum and can be calculated by the following equation[40]:

$$\mathrm{SNR} = \frac{\Delta\lambda_R}{\mathrm{FWHM}}, \tag{12}$$

where $\Delta\lambda_R$ is the difference in the resonance wavelength corresponding to the refractive index of two adjacent analytes. Figure 15 shows the FOM and SNR for different analyte refractive indexes. With increasing n_a, FOM rises initially and then declines, reaching a maximum of 116.95 RIU^{-1} at $n_a = 1.20$. In the refractive index range, the FOM of the sensor is above 25 RIU^{-1} and both the SNR and FOM exhibit consistent trends and the loss spectrum has high quality.

3.7. *Performance comparison*

To illustrate the advantages of our sensor, Table 1 compares the properties of our sensor with those of recently reported PCF-SPR sensors with gold nanowire structures used for low refractive index sensing.

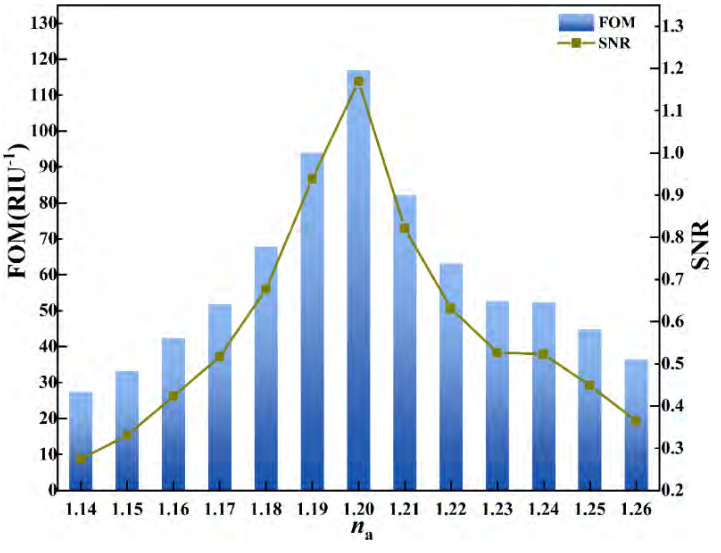

Fig. 15. (Color online) FOM and SNR corresponding to the refractive indexes of different analytes.

Table 1. Comparison of the properties of recently reported PCF-SPR sensors.

Ref.	Characteristics	Max. sensitivity (nm/RIU)	Refractive index range	Resolution (RIU)
19	Gold nanowires outside the PCF	9200	1.33–1.36	2.81×10^{-6}
20	Gold nanowires outside the microfiber	12,314	1.33–1.40	—
39	Gold nanowire in the PCF air hole	10,286	1.32–1.38	9.72×10^{-6}
21	Metal nanowires array on D-type PCF	16,000	1.32–1.38	1.43×10^{-5}
22	Silver nanowires array on D-type PCF; Low refractive index detection	16,400	1.26–1.33	—
41	Gold pillars filled in the PCF pores; Low refractive index detection	X -pol: 5200 Y -pol: 4700	1.21–1.49	—
This work	Gold nanowire outside the PCF; Low refractive index detection	26,000	1.14–1.26	3.85×10^{-6}

4. Conclusion

A ring-core PCF-SPR sensor is designed and demonstrated for low refractive index detection. A gold nanowire is coated on the surface of PCF as the plasmonic medium. The sensor with a simple structure consisting of a central air hole and two layers of cladding air holes is easy to manufacture. In addition, the analyte does not need to be introduced into the interior of the PCF for detection boding well for real-time monitoring in the field. The properties of the sensor are analyzed and the important structural parameters are optimized by the finite element method. The optimized sensor can detect media with high sensitivity in the analyte refractive index range of 1.14–1.26. When the refractive index of the analyte is 1.26, the maximum wavelength sensitivity is 26,000 nm/RIU and the corresponding minimum resolution is 3.85×10^{-6} RIU. The maximum amplitude sensitivity of 300 RIU^{-1} is accomplished when the refractive index of the analyte is 1.19. Furthermore, the maximum detection distance of the sensor is 1187 m rendering the device practical and flexible in real applications. This sensor boasting a large detection range and high sensitivity has immense potential in the detection of low refractive index materials.

Acknowledgments

This work was jointly supported by Heilongjiang Provincial Natural Science Foundation of China [JQ2023F001], the Outstanding Young and Middle-Aged Research and Innovation Team of Northeast Petroleum University [KYCXTD201801], Local Universities Reformation and Development Personnel Training Supporting Project from Central Authorities, Natural Science Foundation of Heilongjiang Province [grant number LH2021F007], China Postdoctoral Science Foundation funded project [grant number 2020M670881], City University of Hong Kong Strategic Research Grant (SRG) [grant number 7005505], and City University of Hong Kong Donation Research Grant [grant number DON-RMG No. 9229021].

References

1. P. Sharma, S. Pardeshi, R. K. Arora and M. Singh, *Int. J. Emerging Technol. Adv. Eng.* **3**(5) (2013) 113.
2. K. K. K. Annamdas and V. G. M. Annamdas, Review on developments in fiber optical sensors and applications, in *Fiber Optic Sensors and Applications VII. SPIE*, Vol. 7677, 2010, pp. 205–216.
3. S. M. Tariq, M. A. Fakhri and U. Hashim, *Key Eng. Mater.* **911** (2022) 65.
4. C. Liu, J. Lv, W. Liu and P. K. Chu, *Chin. Opt. Lett.* **19**(10) (2021) 102202.
5. Y. Chen and H. Ming, *Photonic Sens.* **2** (2012) 37.
6. J. Shibayama, K. Mitsutake, J. Yamauchi and H. Nakano, *Microw. Opt. Technol. Lett.* **63**(1) (2021) 103.
7. L. Li, Y. Liang, J. Guang, W. Cui, X. Zhang, J. F. Masson and W. Peng, *Opt. Express* **25** (22) (2017) 26950.
8. Y. Yuan, L. Ding and Z. Guo, *Sens. Actuators B Chem.* **157**(1) (2011) 240.
9. Y. Zhao, Q. Wu and Y. Zhang, *Measurement* **148** (2019) 106792.
10. E. Liu, S. Liang and J. Liu, *Superlattices Microstruct.* **130** (2019) 61.
11. E. Liu, W. Tan, B. Yan, J. Xie, R. Ge and J. Liu, *J. Phys. D Appl. Phys.* **52**(32) (2019) 325110.
12. C. Li, B. Yan and J. Liu, *J. Opt. Soc. Am. A* **36**(10) (2019) 1663.
13. E. Liu, W. Tan, B. Yan, J. Xie, R. Ge and J. Liu, *J. Opt. Soc. Am. A* **35**(3) (2018) 431.
14. W. Liu, C. Liu, J. Wang, J. Lv, Y. Lv, L. Yang, N. An, Z. Yi, Q. Liu, C. Hu and P. K. Chu, *Results Phys.* **47** (2023) 106365.
15. W. Liu, Y. Shi, Z. Yi, C. Liu, F. Wang, X. Li, J. Lv, L. Yang and P. K. Chu, *Opt. Express* **29**(25) (2021) 40734.
16. W. Liu, C. Hu, L. Zhou, Z. Yi, C. Liu, J. Lv, L. Yang and P. K. Chu, *Physica E Low Dimens. Syst. Nanostruct.* **138** (2022) 115106.
17. C. Liu, H. Fu, Y. Lv, Z. Yi, J. Lin, J. Lv, L. Yang and P. K. Chu, *Optik* **265** (2022) 169471.
18. E. Haque, S. Mahmuda, M. A. Hossain, N. H. Hai, Y. Namihira and F. Ahmed, *IEEE Photonics J.* **11**(5) (2019) 1.
19. X. Yan, B. Li, T. Cheng and S. Li, *Sensors* **18**(9) (2018) 2922.
20. Y. Zhan, Y. Li, Z. Wu, S. Hu, Z. Li, X. Liu, J. Yu, Y. Huang, G. Jing, H. Lu, H. Guan, W. Qiu, J. Dong, W. Zhu, J. Tang, Y. Luo, J. Zhang and Z. Chen, *Opt. Mater. Express* **8**(12) (2018) 3927.
21. K. Tong, Z. Cai, J. Wang and Y. Liu, *Optik* **218** (2020) 165010.
22. H. Pan, C. Cao, A. Zhang, F. Pan, P. Sui and X. Liu, *Optoelectron. Lett.* **18**(7) (2022) 425.
23. W. Liu, C. Hu, L. Zhou, Z. Yi, Y. Shi, C. Liu, J. Lv, L. Yang and P. K. Chu, *Mod. Phys. Lett. B* **36**(1) (2022) 2150499.
24. L. Xu, C. Liu, H. Fu, J. Wang, X. Li, J. Lv, L. Yang and P. K. Chu, *Opt. Eng.* **61**(9) (2022) 096101.
25. T. Okoshi, *Optical Fibers* (Elsevier, 2012).
26. L. Feng, Y. Li, S. Wu, W. Li, J. Qiu, H. Guo, X. Hong, Y. Zuo and J. Wu, *Appl. Sci.* **9**(12) (2019) 2408.
27. W. Liu, C. Hu, L. Zhou, Z. Yi, C. Liu, J. Lv, L. Yang and P. K. Chu, *J. Mod. Opt.* **67**(20) (2020) 1545.
28. S. K. Ghosh and T. Pal, *Chem. Rev.* **107**(11) (2007) 4797.
29. E. Liu, B. Yan, H. Zhou, Y. Liu, G. Liu and J. Liu, *J. Opt. Soc. Am. B* **38**(12) (2021) F16.
30. H. Fu, M. Zhu, C. Liu, Z. Yi, J. Lv, L. Yang, F. Wang, Q. Liu, W. Su, X. Li and P. K. Chu, *Opt. Eng.* **61**(2) (2022) 026111.

31. H. Fu, Z. Yi, Y. Shi, C. Liu, J. Lv, L. Yang and P. K. Chu, *J. Mod. Opt.* **68**(15) (2021) 784.
32. W. Liu, F. Wang, C. Liu, L. Yang, Q. Liu, W. Su, J. Lv, S. An, X. Li, T. Sun and P. K. Chu, *Results Opt.* **1** (2020) 100004.
33. S. Wang, Z. Li, C. Yu, M. Wang, S. Feng, Q. Zhou, D. Chen and L. Hu, *Opt. Mater.* **35**(9) (2013) 1752.
34. S. Wang, S. Feng, M. Wang, C. Yu, Q. Zhou, H. Li, Y. Tang, D. Chen and L. Hu, *Laser Phys. Lett.* **10**(11) (2013) 115802.
35. G. P. Mishra, D. Kumar, V. S. Chaudhary and S. Kumar, *IEEE Sens. J.* **22**(2) (2021) 1265.
36. A. V. Kabashin, S. Patskovsky and A. N. Grigorenko, *Opt. Express* **17**(23) (2009) 21191.
37. N. Luan, R. Wang, W. Lv, Y. Lu and J. Yao, *Sensors* **14**(9) (2014) 16035.
38. H. Fu, C. Liu, C. Hu, L. Zhou, Y. Shi, J. Lv, L. Yang and P. K. Chu, *Opt. Eng.* **60**(7) (2021) 076102.
39. Y. Guo, J. Li, S. Li, Y. Liu, S. Zhang, J. Wang, S. Wang, W. Zhang, T. Cheng and R. Hao, *Optik* **202** (2020) 163671.
40. M. A. Mollah, H. Sarker, M. Ahsan, M. T. Elahi, M. A. Based, J. Haider and S. Palani, *IEEE Access* **9** (2021) 139293.
41. X. Guo, C. Li and J. Cong, *Optik* **271** (2022) 170030.